

Chapter 12

Earth's Bow Shock and Magnetosheath

Aims and Learning Outcomes

The **Aim** of this Chapter is to explore in more detail the physics of fast mode shocks and to introduce the physics of planetary bow shocks and magnetosheaths. This physics links the solar wind with planetary magnetospheres. The emphasis here is on Earth's bow shock and magnetosphere, although the same ideas apply much more widely, both to other magnetospheres but also to travelling shocks.

Expected Learning Outcomes. You are expected to be able to

- Describe and explain qualitatively why shock waves and magnetosheaths develop and what their roles are.
- Describe and explain with reference to the Rankine-Hugoniot equations what the observational signatures of MHD shocks are.
- Understand and explain how the shape and location of planetary bow shocks should vary with the upstream solar wind conditions.
- Describe some purely kinetic aspects of fast mode shocks and explain why they are inconsistent with simple MHD or fluid theory.
- Understand the qualitative physics of gyrating ions and the cross-shock potential and be able to use it to understand aspects of the physics of planetary bow shocks and magnetosheaths.
- Explain qualitatively why the bow shock and magnetosheath are abundant sources of plasma waves and describe some of their consequences.

12.1 Basic Physics of the Bow Shock

The solar wind is both super-Alfvénic and supersonic, with Alfvén Mach number $M_A = v_{sw}/V_A$ and sonic Mach number $M_S = v_{sw}/c_s$ both typically ~ 8 . What happens when the solar wind encounters an obstacle such as a planet's magnetic field, atmosphere or solid surface? In each case the flow must be deflected around the obstacle, either by Lorentz forces or by collisions (mediated by electromagnetic forces). Information on the flow's deflection, however, cannot reach the upstream

plasma via the standard (small amplitude) MHD waves - since the flow is super-Alfvénic and supersonic. Accordingly the deflection must be accomplished by an MHD shock wave.

Figure 12.1 illustrates the relevant plasma regions: the bow shock, which slows, compresses, heats and deflects the solar wind flow; the magnetosheath, in which the shocked solar wind is deflected further around the obstacle and eventually accelerated back up to the solar wind speed (downstream from Earth), eventually merging back into the solar wind where the shock weakens and disappears; the magnetopause, which separates the magnetospheric plasma from the shocked solar wind plasma; and the foreshock upstream of the shock but downstream of the tangent magnetic field lines. The characteristic shapes and boundaries are qualitatively

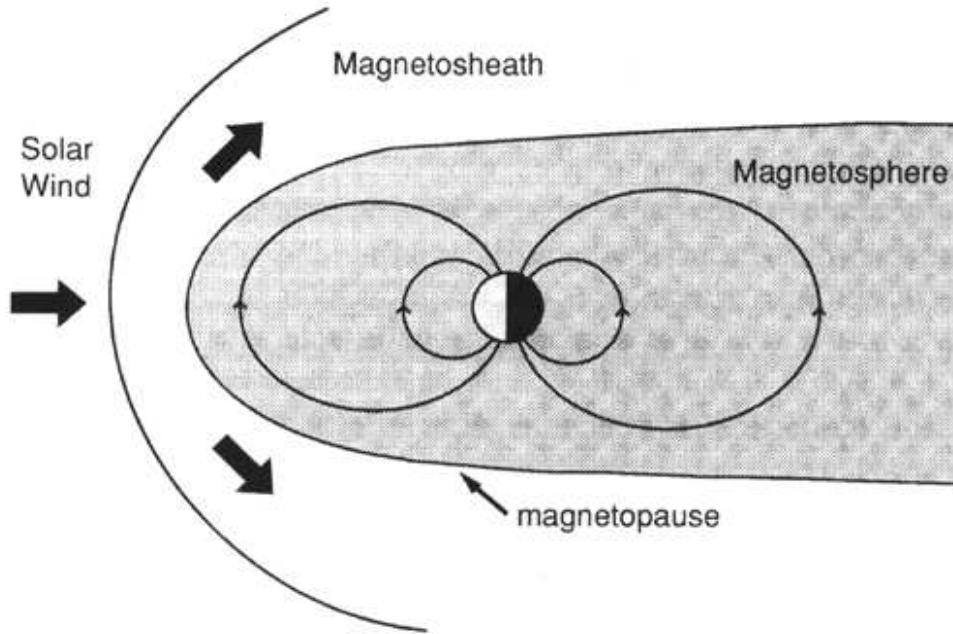


Figure 12.1: Schematic of Earth's bow shock, magnetosheath, and magnetopause [Cravens, 1997].

familiar from the bow waves of ships, bullets, supersonic jets etc.

Qualitatively, a bow shock is just a nonlinearly steepened bow wave. An important aspect of this point is that the propagation speed of many wave modes depends on the wave amplitude (the MHD fast and slow modes and the whistler mode being examples); modes for which the propagation speed increases rapidly enough with wave amplitude can steepen nonlinearly (due to the intense parts of a wave packet piling up) and form shocks and other nonlinear structures such as solitons. One basic difference between solitons and shocks is that shock transitions depend intrinsically on dissipation and an increase in energy across the shock, contrary to the situation for solitons. A shock balances wave nonlinearity against dissipation while a soliton balances the nonlinearity against wave dispersion.

The position and shape of the bow shock depend on the ram pressure

$$P_{ram} = \eta v_{sw}^2, \quad (12.1)$$

Alfvén and sonic Mach numbers, and the angle θ between the solar wind velocity and magnetic field in the solar wind. This can be seen by writing down the MHD

equations in conservative form and then manipulating them. In conservative form the MHD equations can be written:

$$\frac{\partial}{\partial t}(\eta) + \nabla \cdot (\eta \mathbf{v}) = 0 ; \quad (12.2)$$

$$\mathbf{E} = -\mathbf{v} \times \mathbf{B} ; \quad (12.3)$$

$$\frac{\partial}{\partial t} \left[\eta v_i + \frac{1}{\mu_0 c^2} (\mathbf{E} \times \mathbf{B})_i \right] + \nabla_j \left[\eta v_i v_j + P \delta_{ij} + \delta_{ij} \left(\epsilon_0 \frac{E^2}{2} + \frac{B^2}{2\mu_0} \right) - \epsilon_0 E_i E_j - B_i B_j / \mu_0 \right] = 0 \quad (12.4)$$

and

$$\frac{\partial}{\partial t} \left[\eta v^2 + \frac{P}{\Gamma - 1} + \frac{\epsilon_0 E^2}{2} + \frac{B^2}{2\mu_0} \right] + \nabla \cdot \left[\frac{1}{2} \eta v^2 \mathbf{v} + \frac{\Gamma}{\Gamma - 1} P \mathbf{v} + \frac{\mathbf{E} \times \mathbf{B}}{\mu_0} \right] = 0 . \quad (12.5)$$

Normalising throughout by $\mathbf{v} = v_0 \mathbf{v}'$, η_0 , B_0 , etc., in time-invariant systems these equations can be rewritten as

$$\eta_0 v_0^2 \nabla \cdot (\eta' \mathbf{v}') = 0 , \quad (12.6)$$

$$E_0 \mathbf{E}' = -v_0 B_0 \mathbf{v}' \times \mathbf{B}' , \quad (12.7)$$

$$\eta_0 v_0^2 \nabla_j \left[\eta' v'_i v'_j + M_S^{-2} P' \delta_{ij} + \delta_{ij} \left(\frac{v_A^2}{c^2} f_1(\theta) E'^2 + M_A^{-2} B'^2 \right) - \frac{v_A^2}{c^2} f_1(\theta) E'_i E'_j - M_A^{-2} B'_i B'_j \right] = 0 , \quad (12.8)$$

and

$$\eta_0 v_0^2 \nabla \cdot \left[\mathbf{v}' \left(1 + M_S^{-2} \frac{\Gamma}{\Gamma - 1} P' \right) + M_A^{-2} \mathbf{E}' \times \mathbf{B}' \right] = 0 . \quad (12.9)$$

From Eqs (12.6) – (12.9) it can be seen that the overall ram pressure $P_{ram} = \eta_0 v_0^2$ becomes a scale factor for the system and that the equations are otherwise only functions of M_{A0} , M_{S0} , v_A/c , and the angular variables. This is very important because it means that widely applicable results can be obtained using an understanding built up from a few calculations with different P_{ram} , M_A , M_S , and angular variables.

The position and shape of Earth's bow shock, as well as the nature of the shock transition, depend on P_{ram} , M_A , M_S , and the angle θ between the upstream flow velocity and magnetic field [e.g., Spreiter et al., 1966; Cairns and Lyon, 1995]. The overall scale of the bow shock - magnetopause system is obtained by balancing the solar wind ram pressure against the magnetic pressure of Earth's dipole at the magnetopause, i.e.,

$$\eta_0 v_{sw,0}^2 \sim \frac{B^2(r_{mp})}{2\mu_0} \propto A r_{mp}^{-6} . \quad (12.10)$$

That is, the standoff distances for the magnetopause and bow shock (and by extension their transverse scales) vary as $P_{ram}^{-1/6}$. Thus, as expected from intuition, higher ram pressures compress the magnetosphere and bring the bow shock closer to Earth, while lower P_{ram} lead to the opposite effects.

The effects of variations in M_A and M_S are also relatively easy to see qualitatively. For lower Mach number the wave speed is larger relative to the flow speed, so that a wave will travel further upstream in a given nonlinear steepening time, implying that the shock will be found further upstream. Thus, for high M_A the shock is closer to Earth and for low M_A it moves further from Earth. Changes in shock shape are also easy to understand based on the concept of the Mach cone (Figure 12.2), which is the locus of the maximum extent of a disturbance moving away from the obstacle at the wave speed. The Alfvén Mach cone angle is given by

$$\theta_A = \sin^{-1} \left(\frac{V_A}{v_{sw}} \right) = \sin^{-1} (M_A^{-1}) . \quad (12.11)$$

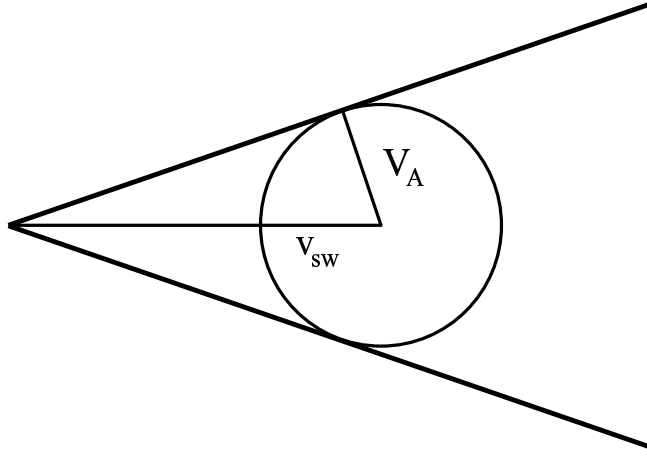


Figure 12.2: A disturbance moves out isotropically at V_A but is carried downstream at v_{sw} . The tangent to the circle from the initial point defines the Alfvén Mach cone.

Thus, the shock shape becomes blunter for smaller M_A and more swept back for larger M_A . This is consistent with simple intuition for a slower and faster flow, respectively.

Figure 12.3 illustrates the changes in the shock's shape and location with variations in M_A . Note that the shock's nose moves sunward as M_A decreases while the shock's shape becomes increasingly blunt, as predicted from Eq. (12.11).

One implication of the solar wind's time-varying characteristics and the dependence of the bow shock's location and shape on P_{ram} , M_A , and M_S is that the bow shock is almost always moving; it is a dynamic object. Times when it is almost stationary are rare and therefore important for studies of the shock's intrinsic structure.

12.2 Fast Mode Nature of Earth's Bow Shock

Figure 12.4 demonstrates that Earth's bow shock is a fast mode shock. Why? Because the plasma is slowed, heated, compressed (ruling out an intermediate/Alfvén shock), and the magnetic field is increased in strength (ruling out a slow mode shock) and changed in direction. The deflection of the flow in velocity is also important, since it is the first step in deflecting the flow around the magnetosphere. Note the small spatial scale of the shock ramp – data similar to Figure 12.4 demonstrate that the spatial scale is of order $10c/\omega_{pe}$, corresponding to about 20 km and approximately $2000\lambda_D$.

Figure 12.5 shows the data for two other crossings of Earth's bow shock, while Figure 12.6 compares the fluid variables with the predictions of the MHD Rankine-Hugoniot conditions, accomplished by nonlinear least-squares fitting of the observations to the theory in order to determine the normal direction and other characteristics of the shock [e.g., Lepidi et al., 1997]. As can be seen, the observations agree well with the theory.

The first indication that the MHD picture is too simple is apparent when one considers the shock heating of the ions and electrons separately. One finds that approximately 90% of the shock heating goes into the ions, with only about 10% going into the electrons, resulting in the condition $T_i \gg T_e$ being satisfied downstream from the shock. Second, most of the ion heating is perpendicular to the

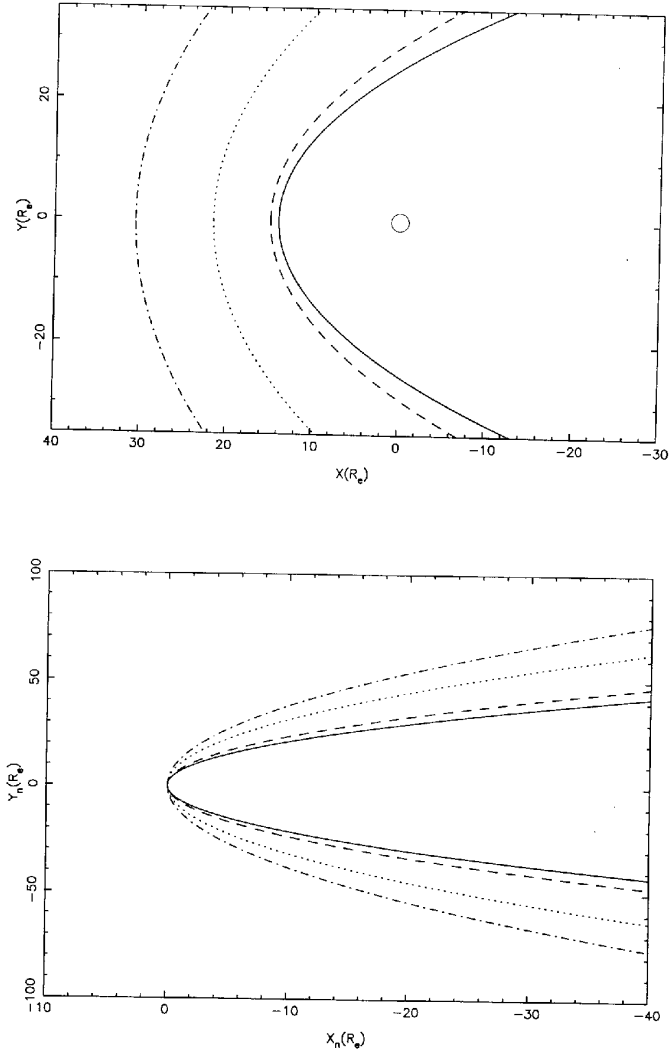


Figure 12.3: Changes in the shock's shape and location with variations in M_A [Chapman & Cairns, 2003]: (top) absolute location relative to the Earth, (bottom) curves shifted so that each shock's nose is at the origin. Here $M_A = 9.7$ (solid curves), 4.9 (dashed), 1.9 (dotted), and 1.4 (fancy).

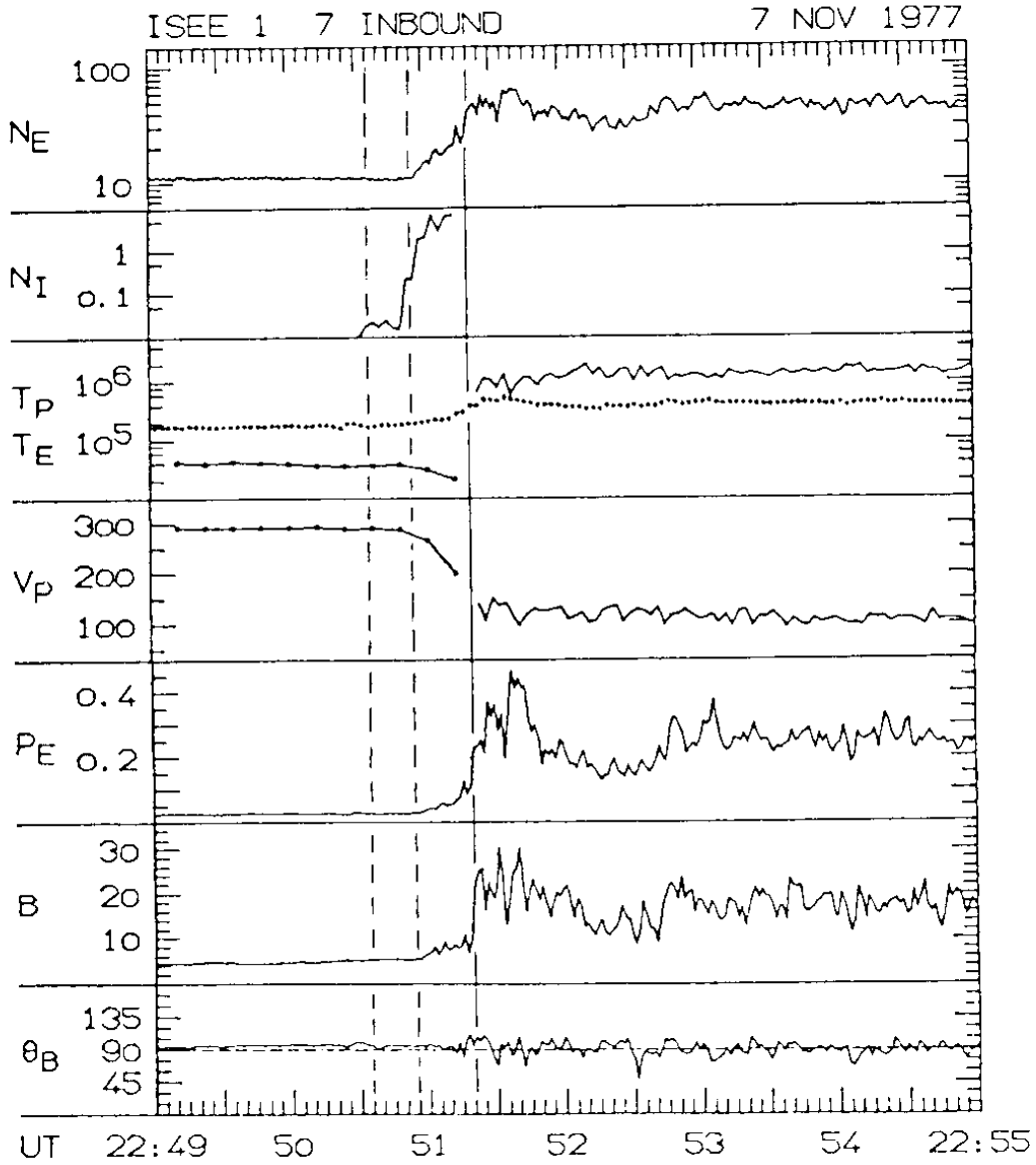


Figure 12.4: Crossing of Earth's bow shock in a region where the shock is quasi-perpendicular and supercritical [Schopke et al., 1983]. The figure demonstrates that Earth's bow shock is a fast mode shock, as well as showing the presence of gyrating ions in the shock's foot.

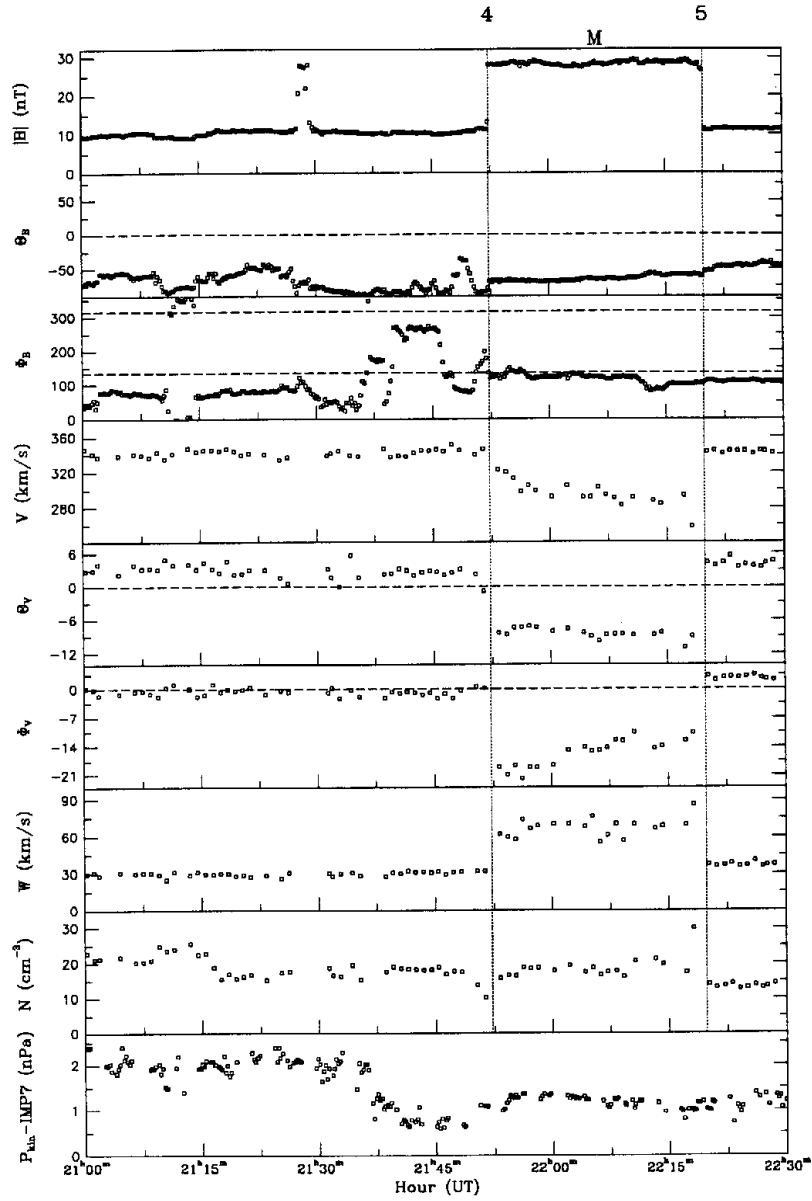


Figure 12.5: Traversal of Earth's bow shock into the magnetosheath near 21:53 with a subsequent return into the solar wind near 21:53 magnetosheath [Lepidi et al., 1997]. (An additional in-out pair is near 21:28.) The shock moves out due to a low density region of the solar wind arriving, and then moves in due to a higher density region, causing the more complicated behaviour of the density.

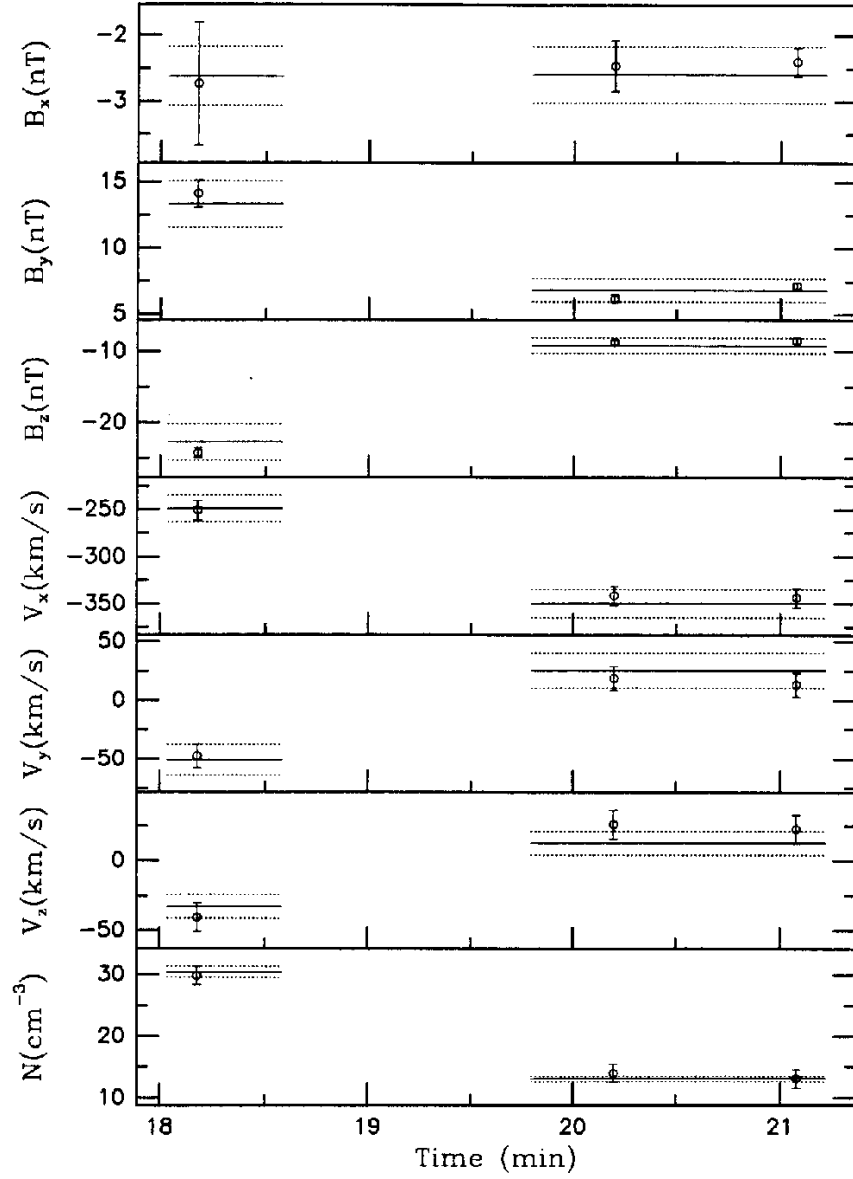


Figure 12.6: Comparison of observational data (open symbols with error bars) for the second shock crossing in Figure 12.5 with predictions based on the Rankine-Hugoniot conditions (solid lines with dashed lines showing the uncertainty limits) [Lepidi et al., 1997].

magnetic field and is much larger than the heating expected just from conservation of the first adiabatic invariant across the shock’s magnetic ramp. Third, the electron heating is primarily consistent with $T_{e,\perp}$ increasing adiabatically across the shock (i.e., constancy of the first adiabatic invariant).

Consider now: “How is the plasma temperature increased in a collisionless shock?”. The answer is easy for a collisional shock: collisions re-distribute the incoming ram kinetic energy as thermal energy. (This explains qualitatively the increase in downstream pressure being proportional to the Mach number squared in the gasdynamic shock in Question 1 of Assignment 2.) But how is this done in a collisionless shock? Not by Coulomb collisions. As suggested by the temperature properties described above, the answer is partially by wave-particle scattering and other kinetic processes that are not included in fluid theories and partially by effects contained in two-fluid theory but not in MHD.

12.3 Kinetic Aspects of Shock Physics

Observations show that the shock structure varies primarily with the fast mode Mach number $M_{ms} = v_{sw}/c_f$ and with the angle θ_{Bn} between the upstream field \mathbf{B} and the local shock normal. In particular, for quasi-perpendicular regions of the shock ($\theta_{Bn} \geq 45$ degrees) there is a transition between “laminar” (smooth) and “turbulent” magnetic profiles in the domain $M_{ms} \sim 2 - 3$, with laminar profiles at low M_{ms} (Figure 12.7). Laminar profiles are by definition smooth, except for upstream trains of standing whistler waves (which are related to dissipation processes at the shock). Turbulent shocks have a well-defined “shock foot”, where the magnetic field smoothly increases over a scale length $\sim v_{sw}/\Omega_p$, and an “overshoot” behind the ramp where the field increases above the Rankine-Hugoniot prediction on a scale $\sim v_{sw}/\Omega_p$ (sometimes with additional ripples) before finally reaching the average field level predicted by the Rankine-Hugoniot conditions. Particle detectors show that the foot and overshoot regions are associated with gyrating beams of solar wind protons reflected at the shock (Figure 12.8). Laminar shock transitions sometimes have an upstream wave train but do not have significant levels of gyrating ions. The production of these gyrating ions is intrinsic to both the structure and dissipation processes active at supercritical shocks, as explained more below. The definition of a “supercritical” shock is that gyrating ions represent the primary dissipation process active at the shock.

Quasi-parallel shocks are very turbulent with fluctuations $\delta B/B_{sw} \sim 1$ and an extensive foreshock region, sometimes to such a degree that it is difficult to identify where the shock transition occurs (Figure 12.9). Large fluxes of gyrating ions are often observed throughout a huge volume near a quasi-parallel shock transition.

The development of reflected, gyrating beams of solar wind ions, with associated creation of foot and overshoot regions and thermalization of the downstream particles is also associated with the self-consistent development of an electrostatic potential across the shock (the “cross-shock potential”). These phenomena can be explained as follows [Gosling et al., 1982; Schwartz et al., 1983; Goodrich, 1985; Scudder et al., 1987].

(1) During one gyroperiod solar wind protons travel about 5000 km (at v_{sw}), while the electrons travel ~ 3 km, and the shock ramp is ~ 20 km thick. The ions thus see the ramp as an abrupt discontinuity during their gyromotion (the ramp is sufficiently thin that they move essentially as unmagnetized particles) while the electrons complete numerous gyroperiods as they cross the ramp.

(2) A self-consistent electrostatic potential is encountered at the shock ramp, which slows and resists the ion flow (but accelerates the electron flow).

(3) A fraction ($\sim 10 - 20\%$) of the solar wind protons have insufficient normal

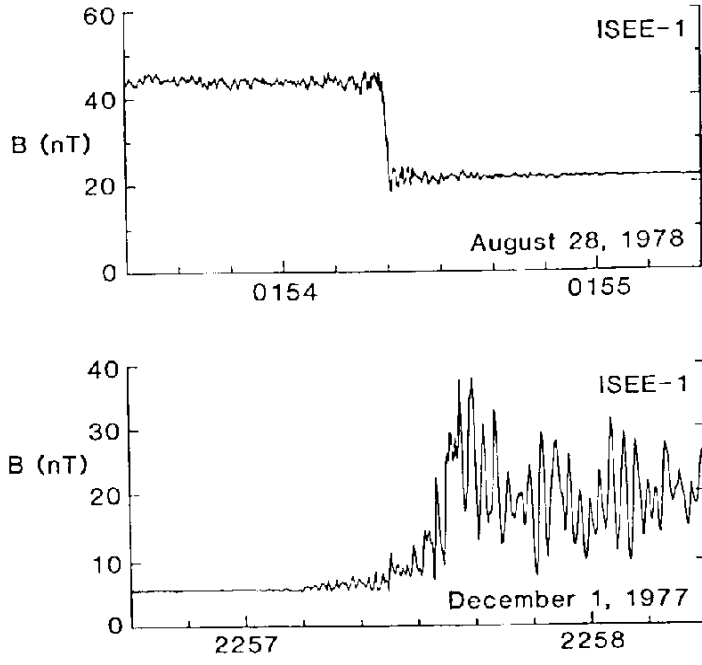


Figure 12.7: The top panel shows a laminar bow shock profile while the bottom panel shows a turbulent shock profile [Livesey et al., 1984; Gosling and Robson, 1985].

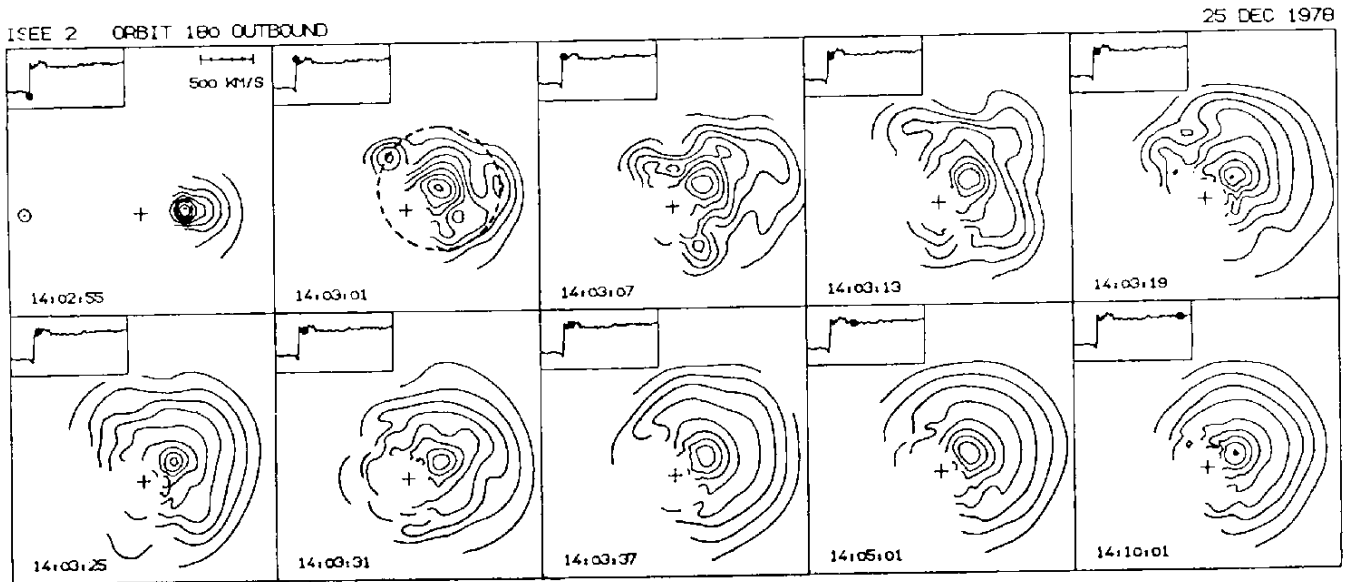


Figure 12.8: Ion velocity distributions observed downstream from a marginally supercritical shock with $\theta_{Bn} \sim 90$ degrees and \mathbf{B} almost perpendicular to the instrument's measurement plane [Schopke et al., 1983]. The dashed circle in the second frame shows the predicted locus for specularly reflected ions.

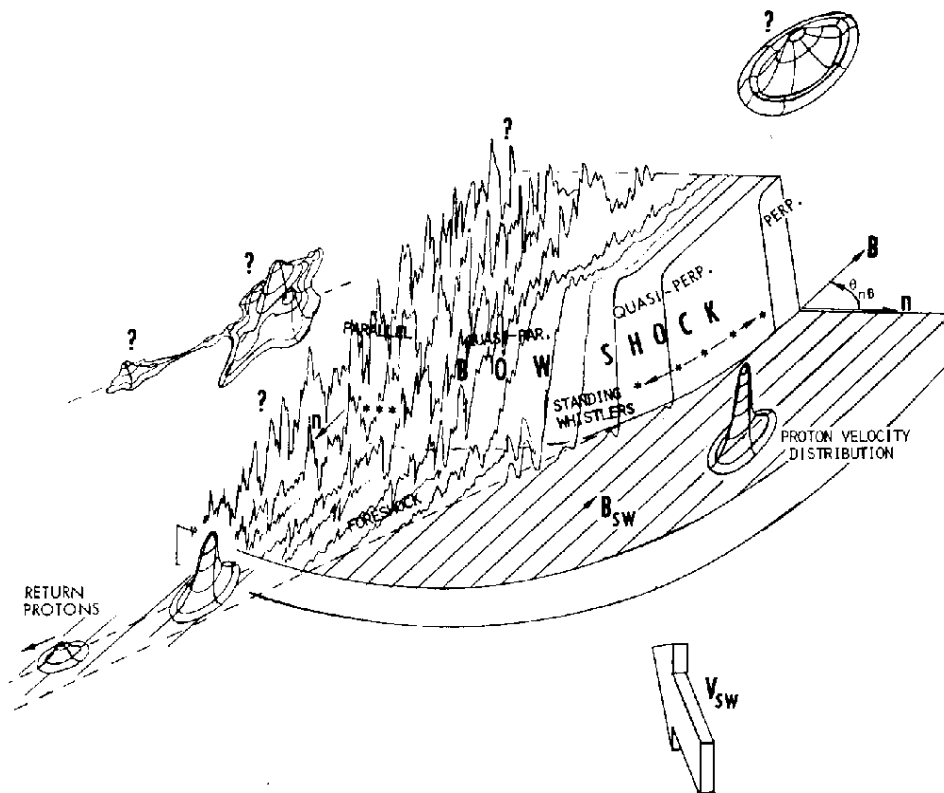


Fig. 1. Conceptualization of collisionless shock macrophenomenology as manifested in the earth's curved bow shock. Unshocked interplanetary field direction B_{SW} is indicated on the foreground field "platform." Field magnitude is plotted vertically; field direction would be deflected somewhat in the B_{SW} plane by the quasi-perpendicular shock, but would share the agitation of the magnitude in the quasi-parallel shock in all components. The superposed three-dimensional sketches represent solar wind proton thermal properties as number distributions in velocity space.

Figure 12.9: Schematic illustration of the quasi-parallel and quasi-perpendicular regions of Earth's bow shock and the foreshock region upstream of the shock [Greenstadt and Fredericks, 1979]. Note that the foreshock region upstream of the quasi-parallel shock is extremely turbulent, often making it difficult to identify the shock transition itself.

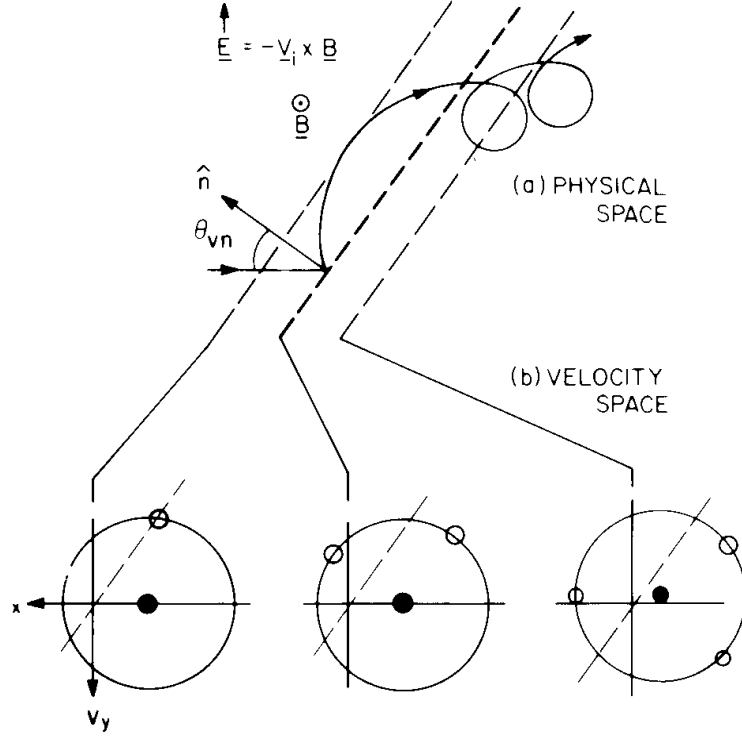


Figure 12.10: Schematic from Gosling and Robson [1985]. (a) Sketch of the trajectory of an ion specularly reflecting off a shock with $\theta_{Bn} = 90$ degrees. (b) Idealized 2-D ion velocity distributions at several distances from the shock ramp. Specularly reflected particles move along a circle of radius $2V \cos \theta_{vn}$ centred at the bulk flow velocity. The dashed lines are aligned parallel to the shock surface.

velocity to overcome the potential barrier and are specularly reflected at the magnetic ramp by the cross-shock potential; that is, their velocities along the normal direction are reversed as shown in Figure 12.10. This is the crucial step in developing the gyrating ions and much of the dissipation across the shock, as described more below. (A similar reflection process leads to “shock surfing” and effective ion acceleration to high energies [Zank et al., 1996].)

(4) The specularly reflected protons move so as to gain energy from the convection electric field and develop a large gyrospeed v_g given by

$$v_g = 2V_i |\cos \theta_{vn} \sin \theta_{Bn}| \quad (12.12)$$

as well as a different gyrocenter velocity. Here $V_i \sim v_{sw}$ is the initial speed in the local shock frame.

(5) The gyrocenter velocity is directed downstream for quasi-perpendicular shocks ($\theta_{Bn} > 45$ degrees) but upstream for quasi-parallel shocks [Gosling et al., 1982].

(6) For quasi-perpendicular shocks, then, the reflected protons gyrate upstream for a partial gyro-orbit before encountering the shock again, now with sufficient normal speed to overcome the potential barrier and pass downstream as a component with large apparent thermal energy. The current associated with this motion causes the magnetic field to increase in the downstream region. The spatial extent of the foot and overshoot are then of order the gyroradius of the specularly reflected ions.

(7) The potential develops as a result of the different motions of electrons and ions. For a perpendicular shock with the normal in the x direction and the magnetic

field in the \mathbf{z} direction, the momentum equation for the electron fluid is

$$m_e n_e \frac{d\mathbf{v}}{dt} = -\nabla P - en_e \mathbf{E} - en_e \mathbf{v} \times \mathbf{B} . \quad (12.13)$$

After neglecting the electron inertia term and performing other manipulations (including writing the electron current in terms of the total current \mathbf{j} and the ion current, using Ampere's Law, and neglecting the displacement current) one may finally write

$$e\phi(x) = \int_{-\infty}^x \frac{dx}{n_e} \frac{\partial}{\partial x} \left(P + \frac{B^2}{2\mu_0} \right) + \int_{-\infty}^x dx V_y B_z . \quad (12.14)$$

The cross-shock potential ϕ thus results from the gradients in thermal and magnetic pressure across the shock (an ambipolar potential) as well as the effects of the net ion drifts associated with the gyrating ions (second term). This potential thus develops self-consistently to allow some ion reflection as part of the shock structure. The cross-shock potential is primarily oriented in the shock's normal direction.

Order of magnitude estimates (see the jump condition (5.12) and the requirement that the potential reflect significant numbers of solar wind ions) are that

$$e\phi \approx \frac{1}{2} m_i v_{sw}^2 \approx k_B T_{i,down} . \quad (12.15)$$

These estimates explain the characteristic size of the cross-shock potential and the amount of ion heating downstream from the shock. Moreover, the above balance between the upstream flow energy and the downstream temperature enhancement also explains qualitatively how the overall Rankine-Hugoniot conditions for the shock transition can be obeyed on the large scale, as they must be despite very different microphysics.

Figure 12.11 shows the development of gyrating ion beams in hybrid simulations (fluid electrons and particle ions), while Figure 12.12 shows the corresponding spatial profiles of the magnetic field strength and the cross-shock potential [Leroy et al., 1983]. Qualitatively the gyrating ions comprise a second ion population moving with significant relative speed to the core solar wind ions, especially perpendicular to the magnetic field. The associated gradients in the particle distribution function imply the possibility of instabilities redistributing this free energy and ending up with a single, broadened and thermalized ion distribution in the magnetosheath. Figures 12.4 and 12.8 show this process observationally [Schopke et al., 1983].

A qualitatively important point is that the cross-shock potential and formation of gyrating ion beams involve reversible physics in the sense that no dissipation, energy loss, or entropy change is involved. How can this lead to an irreversible shock transition with a change in entropy between the upstream and downstream states? The answer is that wave-particle interactions associated with unstable particle distributions lead to dissipation and an increase in entropy. Nevertheless, much of the apparent "heating" of the electrons and ions across the shock can be understood in terms of "reversible" physics and the operation of the cross-shock potential.

A final remark is that for quasi-parallel shocks the gyrating ions have gyrocenters directed upstream from the shock, leading to an extended upstream region filled with gyrating ions and the large-amplitude MHD waves they drive. These upstream "foreshock" regions are then very turbulent with much evidence of Fermi acceleration and wave-particle interactions.

12.4 The Magnetosheath

As illustrated in Figure 12.1 the magnetosheath is the plasma region between the bow shock and the magnetopause in which the shocked solar wind and particles

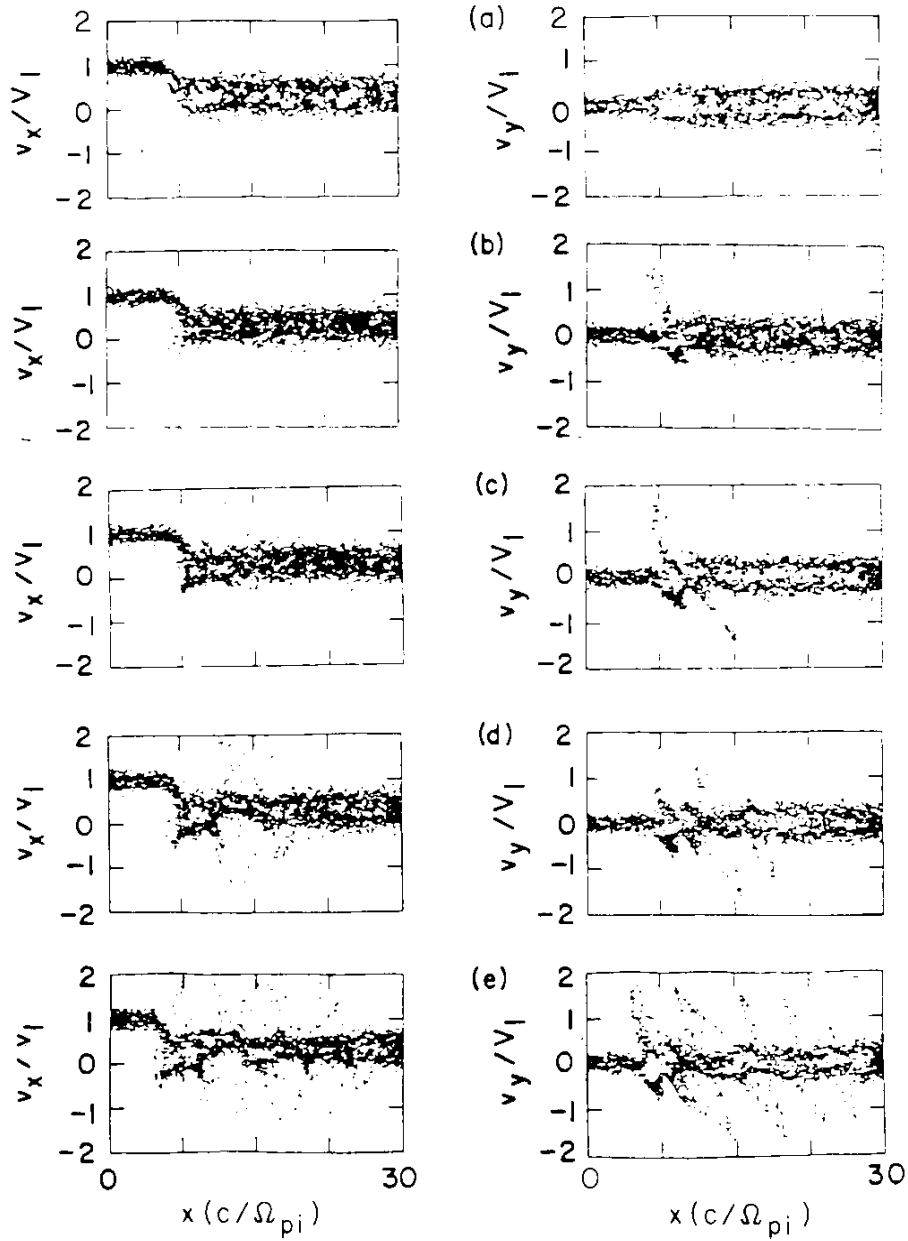


Figure 12.11: Ion phase space plots (v_x, x) and (v_y, x) from hybrid shock simulations [Leroy et al., 1982; Goodrich, 1985]. Here x is the coordinate along the shock normal and the magnetic field is in the z direction, $M_A = 6$, and $\beta_i = \beta_e = 1$. The times for each panel are (a) $t = 0$, (b) $1.3\Omega_{ci}^{-1}$, (c) $2.6\Omega_{ci}^{-1}$, (d) $5.2\Omega_{ci}^{-1}$, and (e) $9.6\Omega_{ci}^{-1}$. Note the development of the gyrating ion beams.

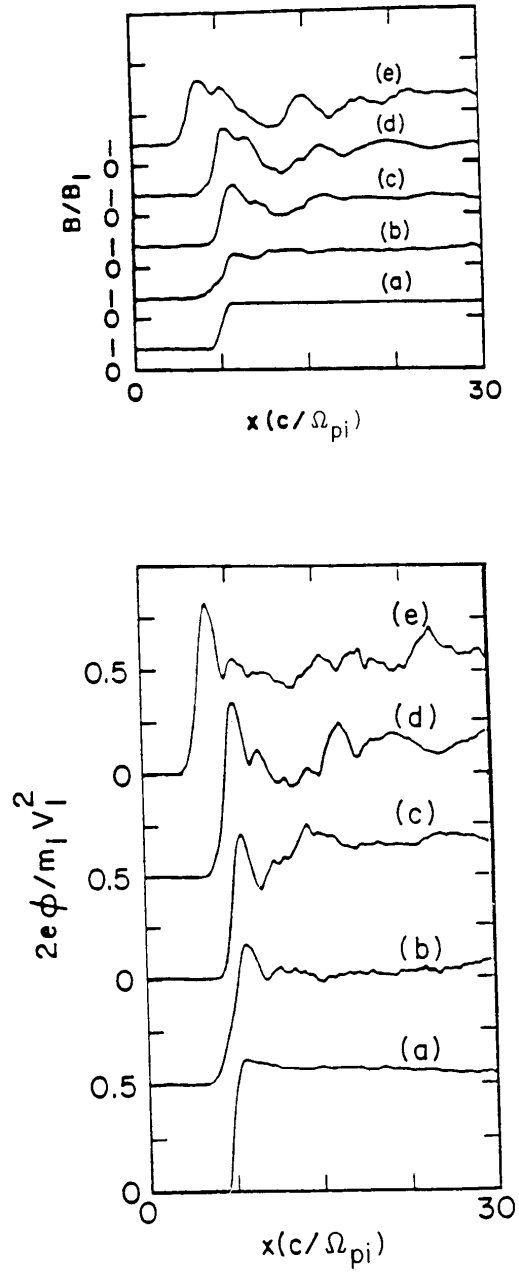


Figure 12.12: Plots of the magnetic field and cross-shock potentials as a function of x and time for the simulations in Figure 12.11 [Leroy et al., 1982; Goodrich, 1985]. Note the development of the foot and overshoot in the potential and magnetic field.

escaping from the magnetosphere are found. Near the nose of the bow shock the magnetosheath plasma is primarily a hot, dense, slow plasma with $T_i \gg T_e$. However, this flow accelerates up towards the solar wind speed and becomes increasingly wind-like toward the flanks of the bow shock, as the shock becomes increasingly weak. MHD and gasdynamic simulations show the large scale structure of the magnetosheath with very good accuracy [e.g., Spreiter et al., 1966]. For instance, Figure 12.13 shows the spatially-varying characteristics of the magnetosheath plasma just described above. Note that the magnetosheath remains a collisionless plasma with collision frequencies much smaller than other relevant frequencies.

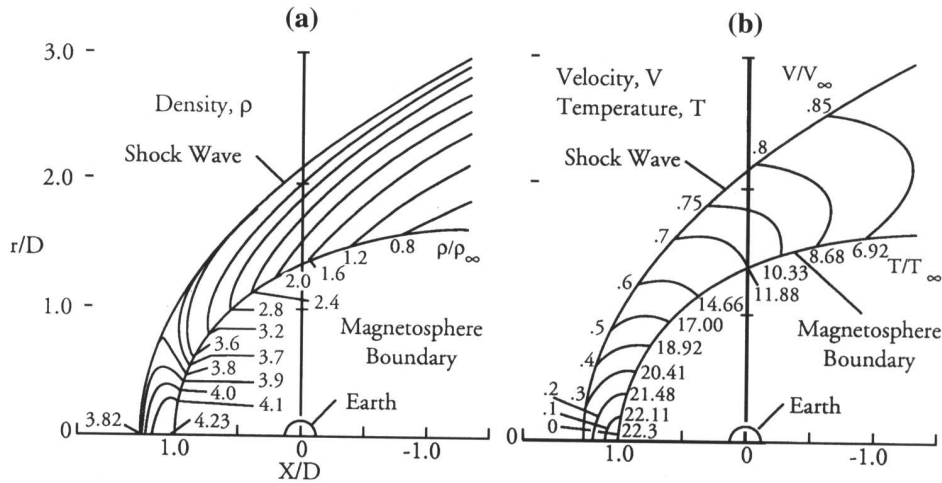


Figure 12.13: Contours of the plasma flow density (left) and both flow speed and temperature (right) in the magnetosheath [Spreiter et al., 1966; Cravens, 1997].

The properties of the bow shock vary with position, leading to changes in the temperature, flow speed, gyrospeed etc. of the particles injected into the magnetosheath. The reason is that the normal speed of the solar wind into the local shock surface varies, causing the local values of M_{ms} , M_A , and M_S to vary and so the Rankine-Hugoniot jumps to vary. These effects can be seen in the varying density, speed and temperature along the shock surface in Figure 12.13.

The particles entering the magnetosheath through the shock have abundant sources of free energy for wave growth due to the ions and electrons both having temperature anisotropies (i.e., $T_{\perp} \neq T_{\parallel}$), due to gyrating ions lying on a ring in velocity space, and due to the cross-shock potential creating a low energy hole in the electron distribution. As discussed qualitatively in Lectures 1, 4 and 11, growth of waves removes energy from the particles, decreases unstable gradients in the particle distribution, and ideally diffuses particles in velocity space and thermalizes the particle distributions by wave-particle scattering.

12.5 References and Bibliography

- Cairns, I.H., and J.G. Lyon, MHD simulations of Earth's bow shock at low mach numbers: Standoff distances, **J. Geophys. Res.**, **100**, 17,173, 1995.
- Chapman, J.F., and I.H. Cairns, Three-dimensional modeling of Earth's bow shock: Shock shape as a function of Alfvén mach number, **J. Geophys. Res.**, **108**, 10.1029/2002JA009569 (SS1, issue A5), 2003.

- Cravens, T.E., *Physics of Solar System Plasmas*, Cambridge, 1997.
- Goodrich, C.C., Numerical simulations of quasi-perpendicular collisionless shocks, in *Collisionless Shocks in the Heliosphere: Reviews of Current Research*, Eds B.T. Tsurutani and R.G. Stone, AGU, p. 153, 1985.
- Gosling, J.T., and A.E. Robson, Ion reflection, gyration, and dissipation at supercritical shocks, in *Collisionless Shocks in the Heliosphere: Reviews of Current Research*, Eds B.T. Tsurutani and R.G. Stone, AGU, p. 141, 1985.
- Gosling, J.T., M.F. Thomsen, S.J. Bame et al., Evidence for specularly reflected ions upstream from the quasi-parallel bow shock, **Geophys. Res. Lett.**, **9**, 1333, 1982.
- Greenstadt, E.W., and R.W. Fredricks, Shock systems in collisionless space plasmas, in *Solar System Plasma Physics Vol. III*, Eds L.J. Lanzerotti, C.F. Kennel, and E.N. Parker, North-Holland, 3, 1979.
- Leroy, M.M., D. Winske, C.C. Goodrich et al., The structure of perpendicular bow shocks, **J. Geophys. Res.**, **87**, 5081, 1982.
- Scudder, J.D., A. Mangeney, C. Lacombe et al., The resolved layer of a collisionless, high β , supercritical, quasi-perpendicular shock wave, Rankine-Hugoniot geometry, currents, and stationarity, **J. Geophys. Res.**, **91**, 11,019, 1986.
- Schopke, N., G. Paschmann, S.J. Bame et al., Evolution of ion distributions across the nearly perpendicular bow shock: Specularly and nonspecularly reflected gyrating ions, **J. Geophys. Res.**, **88**, 6121, 1983.
- Schwartz, S.J., M.F. Thomsen, and J.T. Gosling, Ions upstream of the Earth's bow shock: A theoretical comparison of alternative shock populations, **J. Geophys. Res.**, **88**, 2039, 1983.
- Spreiter, J.R., A.L. Summers, and A.Y. Alksne, Hydromagnetic flow around the magnetosphere, **Planet. Space Sci.**, **14**, 223, 1966.
- Zank, G.P., W.K. Rice, I.H. Cairns, and G.M. Webb, Interstellar pickup ions and perpendicular shocks: Implications for the termination shock and interplanetary shocks, **J. Geophys. Res.**, **101**, 457, 1996.